

# Investigation of Low Discharge Voltage Hall Thruster Operating Modes and Ionization Processes

IEPC-2009-074

*Presented at the 31st International Electric Propulsion Conference,  
University of Michigan • Ann Arbor, Michigan • USA  
September 20 – 24, 2009*

Daniel L. Brown<sup>1</sup>  
*Air Force Research Laboratory, Edwards AFB, CA, 93524, USA*

*and*

Alec D. Gallimore<sup>2</sup>  
*University of Michigan, Ann Arbor, MI, 48109, USA*

**Abstract:** A study of low discharge voltage Hall thruster operation revealed the existence of two operating regimes. Small variations in cathode flow fraction and magnetic field resulted in sharp changes in discharge current with constant thrust, corresponding to a visible change in the jet-mode plume structure. The phenomenon is characterized with a systematic map of thruster operation for discharge voltages ranging from 100 - 120 V, anode flow rates from 10 – 20 mg/s, and cathode flow rates from 7% to 25% of the anode flow. Far-field plume measurements show electron current to the anode is decreased during this transition. The ion energy distributions exhibit significant differences between the high-current and low-current operating modes. These differences are indicative of a significant increase in the fraction of low-energy multiply charged ions and a longer region of primary ion acceleration in the high-current mode.

**DISTRIBUTION STATEMENT A.** Approved for public release; distribution is unlimited.

---

<sup>1</sup> Research Scientist, Spacecraft Branch, Propulsion Directorate, AFRL/RZSS, Daniel.Brown@edwards.af.mil.

<sup>2</sup> Professor, Department of Aerospace Engineering, Associate Dean, Horace H. Rackham School of Graduate Studies, Director, Plasmadynamics and Electric Propulsion Laboratory, Alec.Gallimore@umich.edu.

## Nomenclature

$A_{Effective}$	corrected cross-sectional collection area of the FP collector and gap	[ m <sup>2</sup> ]
$B_{ExB}$	ExB probe magnetic field	[ T ]
$d_{ExB}$	distance between ExB probe parallel plate electrodes	[ m ]
$\mathcal{F}$	Faraday constant	[ 96,485 C/mol ]
$I_{Axial}$	axial component of ion beam current parallel to thruster centerline	[ A ]
$I_{Beam}$	integrated ion beam current	[ A ]
$I_d$	anode discharge current	[ A ]
$I_{probe}$	collected probe current	[ A ]
$I_j$	ion current of the $j$ th ion species	[ A ]
$j$	propellant charge state index = 0, 1, 2, 3 for Xe <sup>0</sup> , Xe <sup>+1</sup> , Xe <sup>+2</sup> , Xe <sup>+3</sup>	[ - ]
$\mathcal{M}$	molecular mass of propellant	[ 0.1313 kg/mol for Xe ]
$\dot{m}_j$	mass flow rate of $j$ th propellant species	[ kg/s ]
$\dot{m}_T$	total propellant mass flow rate to the anode and cathode	[ kg/s ]
$\mathcal{N}_A$	Avogadro's number	[ 6.02x10 <sup>23</sup> particles/mole ]
$n_o$	neutral number density of the facility background gas	[ m <sup>-3</sup> ]
$P_d$	thruster discharge power	[ W ]
$R$	downstream measurement distance from the axis of rotation	[ m ]
$T$	component of thrust vector parallel to thruster centerline	[ N ]
$u_{ExB}$	ion pass speed of the ExB probe	[ m/s ]
$V_{a,j}$	acceleration potential of $j$ th ion species	[ V ]
$V_{Bias}$	probe bias potential	[ V ]
$V_{cg}$	cathode potential relative to facility ground	[ V ]
$V_d$	anode discharge voltage	[ V ]
$V_p$	plasma potential	[ V ]
$v_j$	speed of $j$ th species	[ m/s ]
$X$	translation stage axis in measurement coordinate system	[ - ]
$Y$	translation stage axis in measurement coordinate system	[ - ]
$Z_j$	ion charge state of the $j$ th ion species = 1, 2, 3 for Xe <sup>+1</sup> , Xe <sup>+2</sup> , Xe <sup>+3</sup>	[ - ]
$\gamma_j$	secondary electron emission yield of $j$ th ion species	[ electrons / ion ]
$\eta_T$	total thruster efficiency	[ - ]
$\theta$	angular position, horizontal plane in spherical coordinate system	[ rad ]
$\lambda$	plume momentum divergence half-angle, $\lambda=0$ on thrust axis	[ rad ]
$\sigma_j$	CEX collision cross section of the $j$ th ion species	[ Å <sup>2</sup> ]

## Operations

[R, $\theta$ ]	parameter measured or calculated as a function of R and/or $\theta$
$\langle \dots \rangle_j$	current-weighted average quantity in the plume, at constant R ( $0 < \theta < \pi$ )

## I. Introduction

EARLY investigations in the former Soviet Union observed and characterized Hall thruster discharge oscillations, which are considered an inherent process associated with Hall thruster technology.<sup>1,2</sup> The oscillations are often related to ionization instabilities and density gradients that are dependent on the thruster operation, including variations in discharge voltage, anode mass flow rate, cathode location and mass flow rate, propellant type, thruster geometry, power-processing unit (PPU) characteristics, and magnetic field topography. An exceptional overview of these Hall thruster discharge oscillations ranging from approximately 1-kHz up to over 60-MHz was described by Choueiri.<sup>3</sup>

Several recent investigations have studied complex fluctuations inherent in a Hall thruster discharge, and analyzed thruster operating modes dependent on the thruster operation and design. A systematic study of oscillation behavior from 2-kHz to 100-kHz by Chesta detailed the influence of azimuthal density non-uniformities and probe perturbations, and revealed that the interactions of these effects with the natural Hall thruster discharge dynamics may cause instabilities.<sup>4</sup> A study by Azziz on the BHT-1500 characterized two operating modes that were sensitive

to magnetic field, termed the “jet-mode” and “collimated mode”.<sup>5</sup> These modes were attributed to the location of ionization within the discharge channel, and exhibited variations in ion current density and ion energy distribution in the plume. Extensive studies of Hall thruster dynamics and oscillation behaviors have been conducted throughout the literature, however, the nature of these effects is extremely complex and difficult to quantify.

During the course of low discharge voltage experiments at AFRL with a 6-kW laboratory model Hall thruster, discontinuities in thruster performance occurred for small variations in operating parameters. Minor changes in magnetic field or cathode flow rate resulted in an intense, visible transformation of the jet-mode plume structure. This transformation corresponded to an abrupt escalation in the discharge current with constant thrust and amplification of the discharge oscillations. The transition was achieved with a hysteresis effect, such that identical operation set-points may generate vastly different discharge properties. It has been well documented that low discharge voltage operation is associated with increased oscillation behavior and variation in thruster performance.<sup>6,7</sup> Since the specific nature of the oscillations in this study are unknown, the existence of two discharge operating regimes led to classification as the high-current mode and low-current mode.

In this investigation, the phenomenon is characterized with a systematic map of thruster operation for discharge voltages ranging from 100-V to 120-V, anode mass flow rates at 10-mg/s, 15-mg/s, and 20-mg/s, and cathode flow rate fractions of 7% to 25% of the anode flow. Performance characteristics and far-field plume properties were studied in Chamber 3 at AFRL. Although the exact nature of the operating regimes remains uncertain, the discharge characteristics are evaluated and potential physical causes are discussed.

## II. Plume Visualization of Low Discharge Voltage Operating Regimes

The transition between low discharge voltage operating regimes corresponded to a sudden transformation of the jet-mode plume structure. The plume transformed from an extended, diffuse jet during high-current mode to a more compact jet located further upstream during low-current mode operation. The Hall thruster jet-mode is characterized by a visible jet-like plume profile extending several thruster diameters downstream of the exit, and is distinguished from a diffuse glow discharge by a significantly lower discharge current. Both jet-mode regimes in this study exhibited substantially lower discharge current than operation in the diffuse glow discharge mode. High resolution images of the operating regimes are shown in Figure 1, and contours of constant image intensity more clearly show the extended plume structure in the high-current mode compared to the low-current mode. This qualitative visualization illustrates the extended plume features discernible by eye in laboratory experiments.

During operation near the transition point between the two states, the thruster showed visible signs of flickering and instability. Performance measurements were not taken in this unstable transition regime due to uncertainties in thrust measurements for indeterminate pulsing. The thruster operated in a stable jet-mode in both the high-current and low-current states. As stated previously, the transformation between thruster operating regimes revealed characteristics of hysteresis, where a large cathode flow rate and magnetic field were required to transition from the high-current to low-current regimes. Once the transition to low-current mode occurred, the cathode flow and magnetic field could be decreased while maintaining the decreased current operation.

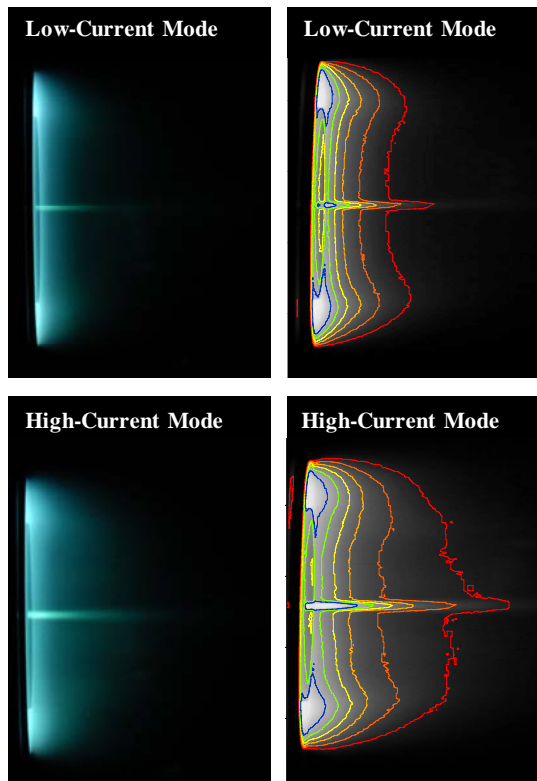


**Figure 1.** Photographs of the 6-kW Hall thruster jet-mode plume structure for the low-current mode (top left) and high-current mode (bottom left) during 105-V, 20-mg/s operation. Contours of constant image intensity are shown for the low-current mode (top right) and the high-current mode (bottom right). Photos were taken with identical settings on a tripod mounted Nikon D200 DSLR using a 70-mm lens with manual focus at F/5, ISO-400, and exposure time of 1/2000 sec.

The extended contours of constant image intensity during high-current mode indicate that excitation and ionization are occurring further downstream in the discharge. In addition, the cathode plume appears more intense and protracts much further from the exit plane. Further investigations are required to develop a better understanding of the interrelated processes driving low discharge voltage Hall thruster operation. In the following sections, the plume properties, performance characteristics, and discharge oscillations will be studied.

### III. Experimental Apparatus

#### A. Thruster

Investigations of low discharge voltage operation in Chamber 3 were conducted with a nominal 6-kW laboratory model Hall thruster with a centrally mounted LaB6 cathode, as shown in Figure 2. The thruster was developed at AFRL in collaboration with JPL and the University of Michigan to serve as a standardized test-bed for research of Hall thruster physics. This 6-kW thruster model has similarities to the P5 and NASA173M thruster designs, and has been characterized at AFRL, PEPL, and JPL.<sup>8,9,10</sup>

The propellant flow system was supplied with research grade xenon (99.999% purity). Anode flow was controlled with a 1000-sccm Unit 1661 digital mass flow controller and cathode flow was regulated with a 100-sccm Unit 8161 digital mass flow controller. An auxiliary flow line with a 1000-sccm Unit 1661 digital mass flow controller was used to increase the facility background pressure by injecting propellant at the chamber floor behind and below the thruster. All mass flow controllers were calibrated with xenon prior to testing with a DH Instruments Molbloc/Molbox gas flow calibration system with an estimated uncertainty of  $\pm 0.5\%$  according to the manufacturer's specifications.

Thruster discharge power was provided by a 1250-V, 80-A AMREL HPS1250-80 DC power supply in line with an RLC circuit to provide low pass filtering of the main discharge. A National Instruments Compact FieldPoint system transmitted thrust and thruster telemetry data to a LabView code monitoring the total thruster efficiency and performance in real-time at  $\sim 10$  Hz. Discharge current oscillations were measured with a CM-10-MG current monitor with a conversion factor of 0.1-V/A. The current monitor was connected to a Tektronix DPO 4034 Digital Phosphor oscilloscope that is rated to 350 MHz. Discharge current was recorded in 100-ns intervals. The dominant discharge frequency is conservatively estimated to within 0.5-kHz.

Prior to experimental measurements, the Hall thruster was run for approximately 3 hours after the initial chamber pump down to allow the system to reach thermal equilibrium. Subsequent thruster warm-up firings were conducted for 1 hour prior to experimental measurements to provide time for the system to out-gas and minimize drift in thrust measurements due to heating of the null coil.

#### B. Vacuum Facility and Measurement Positioning System

The investigation was conducted in Chamber 3 at AFRL, a cylindrical, stainless steel, vacuum chamber 3.3-m in diameter and 8-m in length. The facility utilizes eight helium-cooled cryopanel, resulting in a maximum xenon pumping speed of 140,000 l/s. Background pressure was monitored with two MKS Instruments cold cathode ionization gauges, and facility operating pressures were approximately  $8.0 \times 10^{-6}$ ,  $1.3 \times 10^{-5}$ , and  $1.5 \times 10^{-5}$  torr (corrected for xenon) for xenon anode mass flow rates of 10, 15, and 20-mg/s. Measurements of thrust, discharge current, and current density were conducted at several background pressures to characterize facility effects and minimize measurement uncertainty.

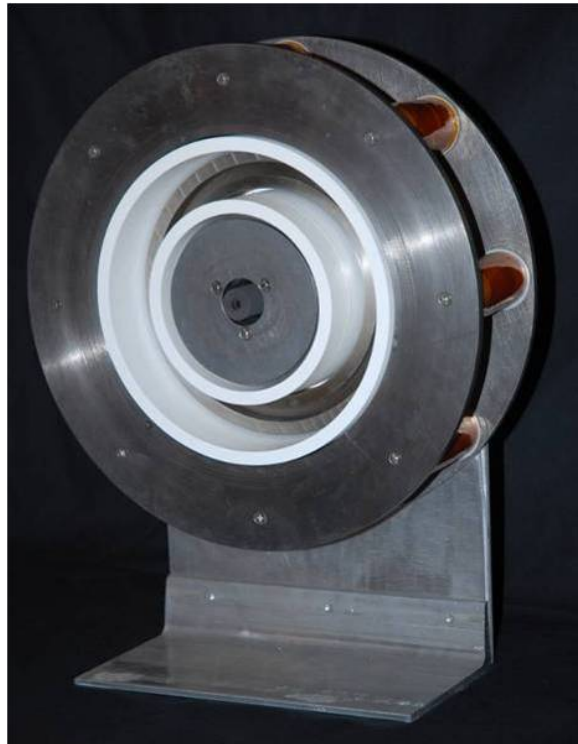


Figure 2. Photograph of the 6-kW laboratory Hall thruster with a centrally mounted LaB6 hollow cathode.

Chamber 3 is equipped with two separate experimental positioning systems. The R- $\theta$  positioning system consists of a rotational arm attached to the chamber ceiling above the thruster exit plane, where the axis of rotation is perpendicular to thruster centerline. The rotational arm was swept in a 1-meter arc from  $\theta=0^\circ$  to  $180^\circ$  and enabled discrete single point measurements or continuous measurements during low-speed travel. Continuous measurements minimized mechanical arm vibrations caused by acceleration and deceleration, and prolonged probe life by decreasing transit time in the plume. A separate X-Y- $\theta$  positioning system was installed that enabled a 1-m by 1-m measurement plane aligned in the thruster centerline horizontal plane. Probe orientation was achieved with a rotation stage that is mounted on X-axis and Y-axis translation stages, with an uncertainty in the probe position of  $\sim 3$  mm relative to the thruster centerline reference point. Further details regarding the AFRL facilities are found elsewhere.<sup>8</sup>

### C. Thrust Stand

Thrust measurements were taken with a null-type, inverted pendulum thrust stand based on the NASA GRC design.<sup>11</sup> The thruster is shown mounted to the thrust stand in Figure 3. Variation in the coil response due to thermal drift was minimized with coolant lines on the copper shroud flowing diluted Glycol solution.

The null type thrust stand utilizes a PID controller with null coil feedback to maintain stationary thruster position. Thrust stand calibration was conducted with a set of five known weights in a pulley system assembly, and the null coil response was correlated to the exerted force. As the thrust stand and thruster reached thermal equilibrium, the calibration curves showed repeatability with less than 1% variation. The zero offset was recorded after each test point and used with the calibration slope to calculate thrust. In cases where the thrust stand was not calibrated after each operating condition, the zero position was found for each point in time based on a linear interpolation of the zero offset before firing and after shutdown. At steady state conditions, thrust measurements varied by less than 0.5 mN. Due to the highly repeatable thrust measurements and minimal thermal drift, the overall uncertainty in thrust is conservatively estimated at  $\pm 2\%$ .

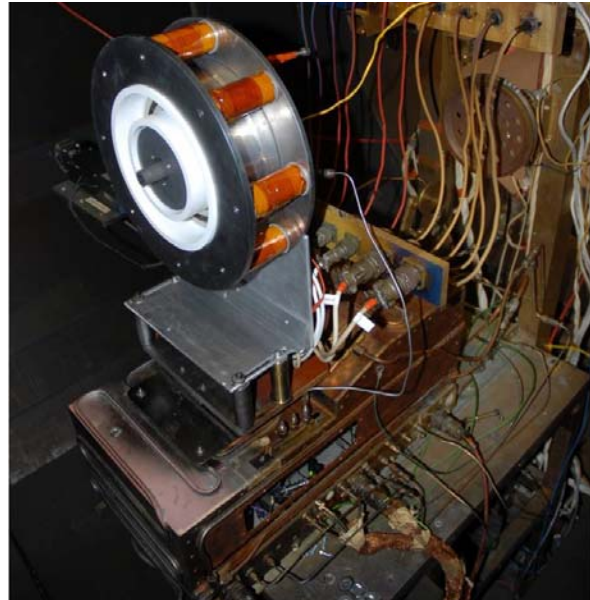


Figure 3. Photograph of the 6-kW Hall thruster on the inverted pendulum thrust stand at AFRL/RZSS.

### D. Nude Faraday Probe

Ion current density of the Hall thruster plume was examined 1-meter downstream of the thruster exit plane as a function of angular position from thruster centerline. The nude Faraday probe, shown on the diagnostic array in Figure 4, is a conventional design that has been used extensively for studies in Chamber 3 at AFRL. The array is positioned by a rotational arm located above the exit plane perpendicular to thruster centerline and swept continuously  $180^\circ$  through the plume.

The Faraday probe electrical circuit and geometric dimensions are shown in Figure 5. The nude Faraday probe measured ion current to a 19.4 mm diameter collector bordered by a 43 mm diameter annular guard ring. The collector to guard ring gap is 1.3 mm, and the collection area is corrected to account for ions collected on the collector side walls.<sup>8</sup> This correction results in a collection area of  $3.24 \text{ cm}^2$ . The bias voltage is set to

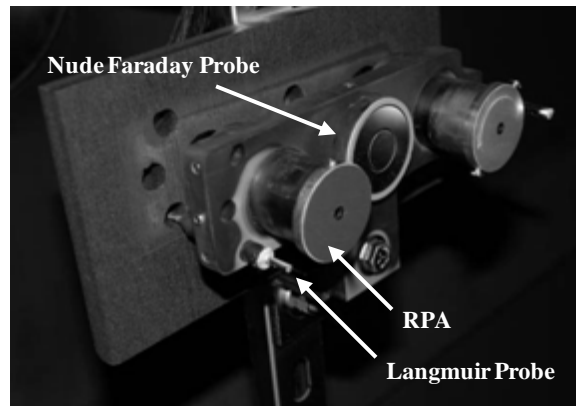
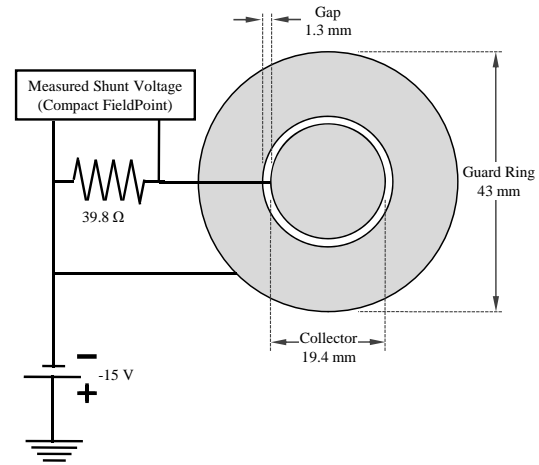


Figure 4. Plasma diagnostic array on the rotational arm at AFRL. Probes from left to right include the Langmuir probe, RPA, nude Faraday probe, and gridded Faraday probe.

-15 V with respect to ground by a Sorenson LT 30-3 DC power supply. Collected current is found from the voltage drop across a 39.6  $\Omega$  shunt resistor, and is recorded with the Compact FieldPoint data acquisition system. The guard ring is biased to the same negative potential as the collector and forms a uniform, planar sheath in front of the collection area. Data analysis and measurement techniques follow the guidelines developed based on a nested Faraday probe design previously studied at AFRL.<sup>8,12</sup> The resulting uncertainty in integrated ion beam current is estimated at  $\pm 3\%$ .

The ion beam current is calculated through integration of ion current density at constant radius throughout the thruster plume. In Eq. (1) and Eq. (2), the measured current densities from each side of the plume ( $0^\circ$  to  $90^\circ$  and  $90^\circ$  to  $180^\circ$ ) are integrated, and the reported beam currents are the average of the two sides. Repeated scans show excellent precision.



**Figure 5. Electrical diagram of the nude Faraday probe power electronics and DAQ system.**

$$I_{\text{Beam}} = 2\pi R^2 \int_0^{\pi/2} \frac{I_{\text{probe}}[\theta]}{A_{\text{Effective}}} \sin(\theta) d\theta \quad (1)$$

$$I_{\text{Axial}} = 2\pi R^2 \int_0^{\pi/2} \frac{I_{\text{probe}}[\theta]}{A_{\text{Effective}}} \cos(\theta) \sin(\theta) d\theta \quad (2)$$

An effective plume divergence angle,  $\lambda$ , may be calculated as the shown in Eq. (3). This angle is significantly less than the 95% divergence half-angle that is typically reported for evaluation of plume expansion.

$$\lambda = \cos^{-1} (\langle \cos(\theta) \rangle_J) = \cos^{-1} \left( \frac{I_{\text{Axial}}}{I_{\text{Beam}}} \right) \quad (3)$$

### E. Langmuir Probe

A single, cylindrical Langmuir probe was used to measure plasma potential near the retarding potential analyzer (RPA) in order to accurately evaluate the far-field average ion acceleration potential. The Langmuir probe consisted of a 0.5 mm diameter, 10 mm length tungsten wire protruding from a 3.2 mm (1/8 inch) diameter alumina tube. Bias voltage relative to facility ground was applied to the wire electrode by a Keithley 2400 Sourcemeter and recorded with LabView on a data acquisition computer.

The Langmuir probe was mounted to the diagnostic array in Figure 4 and aligned toward the rotational arm axis of rotation. The Langmuir probe electrode was positioned 1 meter downstream of the thruster exit plane at  $\theta=90^\circ$ , approximately 3-cm to the side of the RPA. Prior studies concluded the far-field plasma potential varies by only a few volts across large angles.<sup>13</sup> Due to the proximity of the Langmuir probe to the RPA, the difference in plasma potential between the Langmuir probe location and the RPA on the thruster centerline was estimated at less than one volt. Plasma potential was estimated based on curve fitting to the “knee” in the measured I-V characteristic curve and also using the peak in the first derivative of collected current as a function of bias voltage. The two methods differed in measured plasma potential by less than 2 V for all cases. The overall uncertainty in measured plasma potential at the RPA location was estimated at  $\pm 3$  V, which includes error in data analysis and variation due to the Langmuir probe distance from the RPA.

## F. Retarding Potential Analyzer

A RPA measured the ion voltage distribution by controlling the minimum ion energy per charge to a collector with a series of positively and negatively biased grids. The grid configuration is shown in Figure 6, and the bias voltages and separation distance are listed in Table 1. The RPA is based on the gridded energy analyzer design described by Hutchinson<sup>14</sup> and has been used extensively for studies in Chamber 3 at AFRL.

The outer grid (Grid 1) exposed to the plume is floating to minimize the perturbation between the probe and ambient plasma. Electron repelling Grids 2 and 4 are biased to -30 V below facility ground by a BK Precision 1760 Triple Output DC power supply. The ion retarding Grid 3 is connected to a Keithley 2410 1100-V Sourcemeter and swept from 0 V to 150% of the discharge voltage with respect to facility ground. The retarding grids filter ambient electrons and selected ions before they reach the copper collector of the RPA. A Keithley 485 Picoammeter recorded the RPA collected current with respect to facility ground. Data acquisition of the applied ion retarding potential and collected RPA current was controlled on a computer running LabView. Retarding grids are composed of a 0.127-mm thick, photochemically etched 316 SS with an open area fraction of approximately 38% and separated by MACOR spacers.

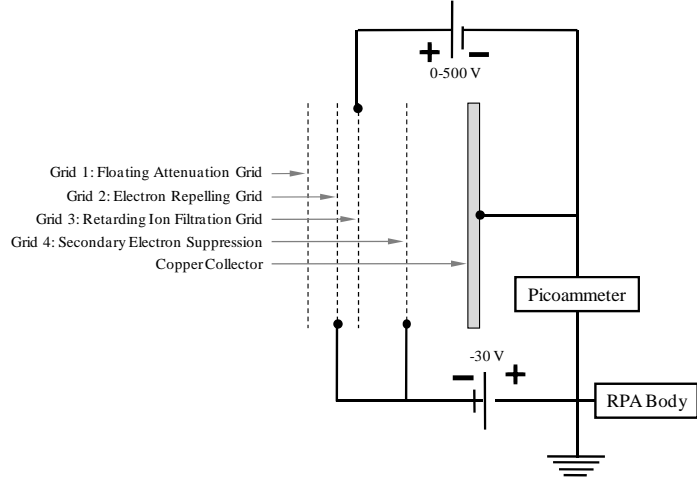


**Figure 6. Electrical diagram of the RPA grid power electronics and DAQ system.**

**Table 1. RPA grid bias potentials and grid separation**

	Bias Potential (to facility ground) [ V ]	Grid Separation [mm]
Grid 1: Floating Grid	Floating	3.35 (Grid 1-2)
Grid 2: Electron Repelling Grid	- 30 V	1.73 (Grid 2-3)
Grid 3: Ion Retarding Grid	0 to 1.5V <sub>d</sub>	6.55 (Grid 3-4)
Grid 4: Secondary Electron Suppression Grid	-30 V	6.55 (Grid 4 – Collector)

The derivative of the measured I-V characteristic is proportional to the ion energy per charge distribution, and is shown in Eq. (4) for a plasma with a single ion species such that  $I_{\text{Probe}}=I_j$  and  $f(V_{\text{Bias}})=f(V_{a_j})$ . Although the distribution function magnitude has significant uncertainty, the location of the peak in the ion voltage distribution is a high fidelity measurement and repeated traces demonstrated excellent precision. The most probable ion potential in the  $dI/dV$  trace may be used to establish a local average ion acceleration potential of all ion species. RPA data was processed in the IGOR Pro software environment. Raw collected current data was fitted with a cubic spline prior to differentiation to reduce signal noise.

$$\frac{dI_{\text{Probe}}}{dV_{\text{Bias}}} = \frac{dI_j}{dV_{a_j}} = -n_j Z_j^2 f(V_{a_j}) \left( \frac{A_c}{\mathcal{N}_A \mathcal{M}} \mathcal{F}^2 \right) \quad (4)$$

## G. ExB Probe

In the ExB probe, perpendicular electric and magnetic fields establish an ion velocity filter and thereby discern the relative ion species composition in the plume. The ion velocity filter is established by balancing the perpendicular electromagnetic forces in the Lorentz force equation, such that there is no net force acting on particles with a select velocity normal to the applied electric and magnetic fields. Ions with an entrance velocity different than the filter pass velocity ( $u_{\text{ExB}}$ ) experience a non-zero drift force and are deflected from the collector.

The ExB probe functions solely as an ion velocity filter, and the measured ion velocity distribution is independent of mass and charge. Hall thruster plumes are typically composed of multiple ion species, where each ion species is created within a narrow region of the discharge channel such that the exit velocity is proportional to the square root of the ion charge state,  $Z_j^{1/2}$ . In Eq. (5), ExB probe ion pass velocity is related to the individual ion species velocity ( $v_j$ ) and the local plasma potential ( $V_p$ ).

$$u_{\text{ExB}} = v_j + \sqrt{2 Z_j V_p \left( \frac{\mathcal{F}}{\mathcal{M}} \right)} = \sqrt{2 Z_j (V_{a,j} + V_p) \left( \frac{\mathcal{F}}{\mathcal{M}} \right)} = \frac{V_{\text{Bias}}}{B_{\text{ExB}} d_{\text{ExB}}} \quad (5)$$

The local plasma potential must be included in this formulation due to the finite ion acceleration between the plasma potential at the inlet orifice and the facility ground used to reference the plate bias potential. Knowledge of the distance between the plates ( $d_{\text{ExB}}$ ) and the fixed magnetic field ( $B_{\text{ExB}}$ ) enables a relationship between the applied electrode bias voltage ( $V_{\text{Bias}}$ ) and the ion pass velocity as a function of particle species, charge state, plasma potential, and the ion acceleration potential ( $V_{a,j}$ ).

As opposed to the energy per charge distribution measured by the RPA, each ion species will correspond to individual peaks in the ExB velocity distribution and may be identified based on the respective ion mass and charge state. The contribution of each ion species to the total collected current is expressed in Eq. (6), and is related to the ion species mass flow rate ( $\dot{m}_j$ ) and ion species number density ( $n_j$ ). The secondary electron emission yield term ( $\gamma_j$ ) is neglected in this study, since the ExB probe collector assembly includes an electron suppression grid upstream of the collector.

$$I_j = \dot{m}_j Z_j \left( \frac{\mathcal{F}}{\mathcal{M}} \right) (1 + \gamma_j) = n_j Z_j v_j A_c \left( \frac{\mathcal{F}}{\mathcal{N}_A} \right) (1 + \gamma_j) \quad (6)$$

The ExB probe in this investigation was designed and manufactured by Plasma Controls, LLC.<sup>15</sup> In the Plasma Controls design, the distance between the parallel plate electrodes is 3.1 mm and the magnetic flux density is 0.344 T. The entrance collimator orifice is ~0.4 mm diameter, which provides an acceptance angle of approximately  $\pm 0.3^\circ$ . The ExB probe was aligned in the plume using the X-Y- $\theta$  positioning system described in Section III.B.

The ExB bias parallel plates were connected to a Keithley 2410 1100-V Sourcemeter and swept from 0 to ~50 V with respect to the probe body and facility ground. During low discharge voltage thruster operation, the maximum sweep voltage was set based on the expected probe bias potential required to measure  $\text{Xe}^{+3}$  ions. An electrical schematic is shown in Figure 7. A secondary electron suppression grid was biased to -30 V below thruster ground with a BK Precision 1760 Triple Output DC power supply. A Keithley 6485 Picoammeter recorded the collected current with respect to facility ground, with Average and Median filters enabled. Data acquisition was controlled on a computer running LabView, and voltage sweeps took several minutes each due to the signal averaging. No post-processing or smoothing was required.

Systematic studies of ExB probe spectra at various downstream distances and angles concluded that a single-point measurement on channel centerline provided an accurate assessment of the ion composition in the plume compared to a multi-point spatial map.<sup>16</sup> Repeated ExB measurements of ion velocity distribution showed excellent precision, and species current fractions were determined using the method of triangle fitting. A methodical comparison of various ExB analysis techniques by Shastry<sup>16</sup> demonstrated the method of triangle fitting captured the effects of peak width on the calculated ion species composition in accord with more complicated curve-fitting procedures.

Beam attenuation due to CEX collisions is accounted for using a simplified model that has been shown to accurately modify the ion species

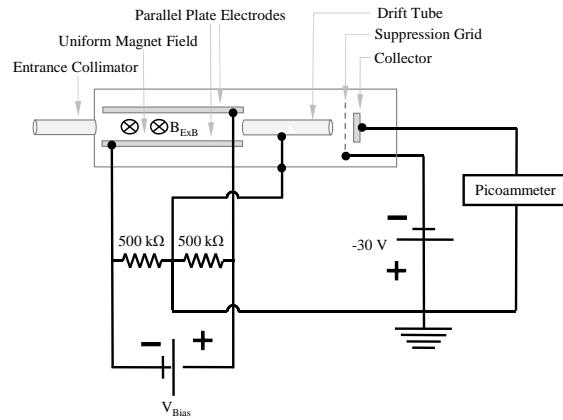


**Figure 7. Electrical diagram of ExB probe power electronics and DAQ system.**

current fractions for symmetric reactions between beam ions and a uniform background neutral density.<sup>16</sup> The CEX attenuation is calculated for a given ion species as shown in Eq. (7) and the respective CEX collision cross sections are listed in Eqs. (8) through (10).

$$\left( \frac{I_{\text{probe}}[\text{R}]}{I_{\text{probe}}[\text{R} = 0]} \right)_j = \exp(-n_o \sigma_j Z_j) \quad (7)$$

$$\sigma_1 = 87.3 - 13.6 \log(V_d) \quad (8)$$

$$\sigma_2 = 45.73 - 8.9 \log(2V_d) \quad (9)$$

$$\sigma_3 = 16.9 - 3.0 \log(3V_d) \quad (10)$$

The model was stated to work best when the product of background pressure (in  $10^{-5}$  torr) and downstream measurement distance (in meters) was  $\leq 2$ . The maximum ExB probe measurement was taken 1.3-m downstream of channel centerline and the maximum background pressure was  $1.5 \times 10^{-5}$  torr. The criterion ( $1.3 \times 1.5 < 2$ ) was satisfied for ExB probe measurements at all thruster operating conditions. The measurement uncertainty of background pressure is  $\pm 20\%$ , and inserting this range of uncertainty into the estimation of beam attenuation varied the current fraction calculations of  $\text{Xe}^{+1}$ ,  $\text{Xe}^{+2}$ , and  $\text{Xe}^{+3}$  by approximately  $\pm 0.02$ ,  $\pm 0.01$ , and  $\pm 0.005$ , respectively. The overall uncertainty in  $\text{Xe}^{+1}$ ,  $\text{Xe}^{+2}$ , and  $\text{Xe}^{+3}$  current fractions is approximately  $\pm 4\%$ ,  $\pm 20\%$ , and  $\pm 50\%$ , respectively.

## IV. Thruster Performance and Discharge Characteristics

### A. Mapping Thruster Operation for Anode and Cathode Flow Rate

The low discharge voltage thruster operation is examined from 100-V to 120-V in a systematic map of discharge voltage, anode mass flow rate, and cathode mass flow rate. In Figure 8, the thruster operating characteristics are shown for lines of constant discharge voltage as a function of cathode flow fraction at anode flow rates of 10-mg/s, 15-mg/s, and 20-mg/s. This data set has not been extrapolated to vacuum conditions, and magnetic fields were adjusted for maximum efficiency.

At a critical cathode flow fraction, the discharge current dropped by approximately 10%. This reduction is emphasized with arrows, and occurs across the operating transition from the high-current mode to the low-current mode for 100-V to 110-V thruster operation. The performance map features the thruster operating parameters where the low-current mode is achievable for an optimal magnetic field configuration.

Two points should be addressed regarding this performance map. The high-current operating regime also existed for 115-V and 120-V thruster operation in a span of magnetic field settings, but the thruster was capable of operation in the low-current mode for the full range of cathode flow rates studied. Conversely, thruster operation reported in the high-current mode below 110-V was unable to transition to low-current mode, such as during 100-V, 10-mg/s anode flow rate below 24-CFF.

Thrust was relatively constant between the low-current and high-current mode. The linear increase in thrust with cathode flow is attributed to neutral ingestion and acceleration of cathode propellant. As a result of the decline in discharge current associated with the low-current operating regime, the T/P and total thruster efficiency improved. Further increases in CFF generated additional neutral ingestion, and led to further increases in total efficiency for the 20-mg/s operating conditions. The highest T/P occurred for 15-mg/s operation at 26-CFF, however, the trend in the 20-mg/s data set indicates the T/P may also be increased to similar levels if CFF is increased beyond 14-CFF up to 26-CFF. Global observations of low discharge voltage operation from Figure 8 are summarized below.

1. For constant discharge voltage and anode flow rate, decreasing cathode flow fraction to a critical level led to operation in the high-current mode, corresponding to a step-increase in discharge current with approximately constant thrust.
2. Lower discharge voltage operation required a larger cathode flow fraction for thruster operation in the low-current regime (24-CFF at 100-V, 10-mg/s compared to 10-CFF at 110-V, 10-mg/s).

3. Lower anode flow rate operation required a larger cathode flow fraction for thruster operation in the low-current mode (24-CFF at 100-V, 10-mg/s compared to 12-CFF at 100-V, 20-mg/s).
4. The greatest difference in thruster performance between low-current mode and high-current mode occurred for low-voltage, high anode flow rate operation (total efficiency gain of 5.5% at 100-V, 20-mg/s compared to 1.5% gain at 110-V, 10-mg/s).
5. For constant anode mass flow and constant CFF above the critical value for low-current operation, increasing discharge voltage from 100-V to 120-V resulted in improved T/P and nearly constant  $\eta_T$ .

In Figure 9, the low-voltage I-V characteristics of thruster operation at 7-CFF from 100-V to 300-V for 10-mg/s anode flow rate. The low-current mode follows the trend of nominal thruster operation, and the high-current mode appears to be a low discharge voltage anomaly. Thus, reduced cathode flow rate during low-voltage operation leads to a performance detriment. Since thrust is relatively constant during the transition from low-current mode to high-current mode, the simplest mechanism for increased discharge current is an escalation in electron current to the anode. This hypothesis will be evaluated with a Faraday probe in Section V.A.

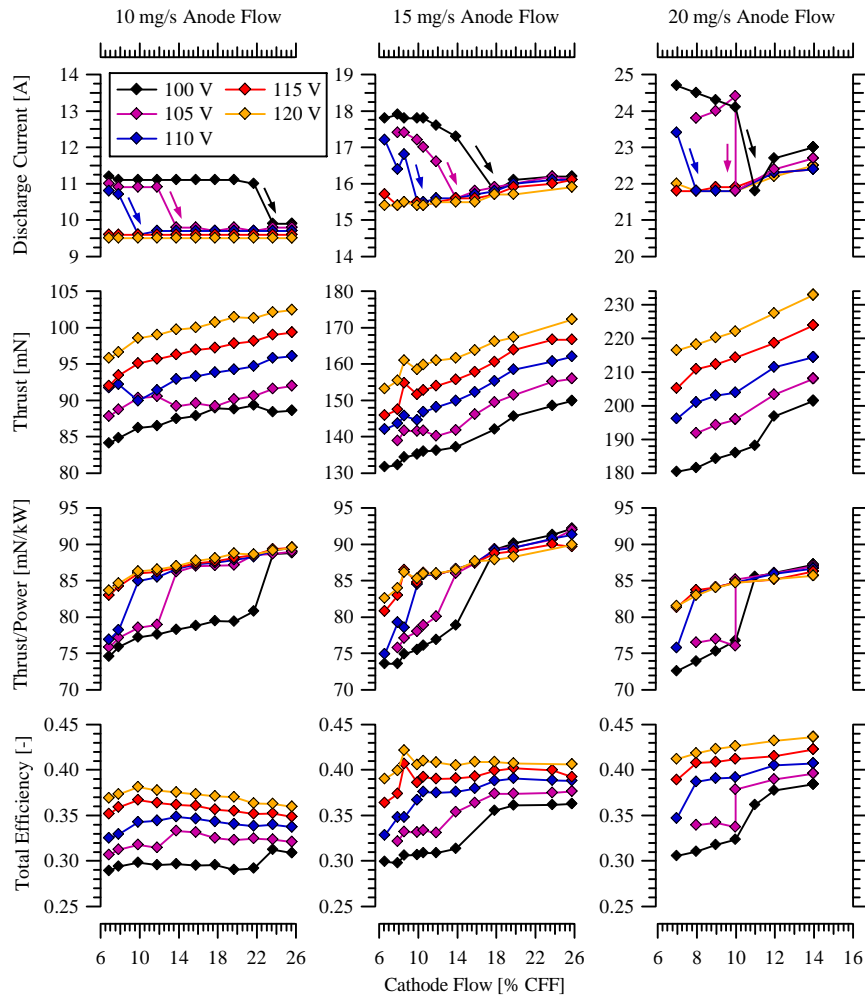


**Figure 8.** Mapping of anode and cathode thruster operating characteristics at 100-V, 105-V, 110-V, 115-V, and 120-V discharge. Discharge current, thrust, thrust to power ratio, and total thruster efficiency are shown for lines of constant discharge voltage as a function of cathode flow fraction during 10-mg/s (left column), 15-mg/s (middle column), and 20-mg/s (right column) anode mass flow rate operation. Operating characteristics are reported for facility background pressure in the range of  $8.0 \times 10^{-6}$  to  $1.2 \times 10^{-5}$  torr. Transitions from the operation in low-current to high-current mode are shown with arrows in the plots of discharge current.

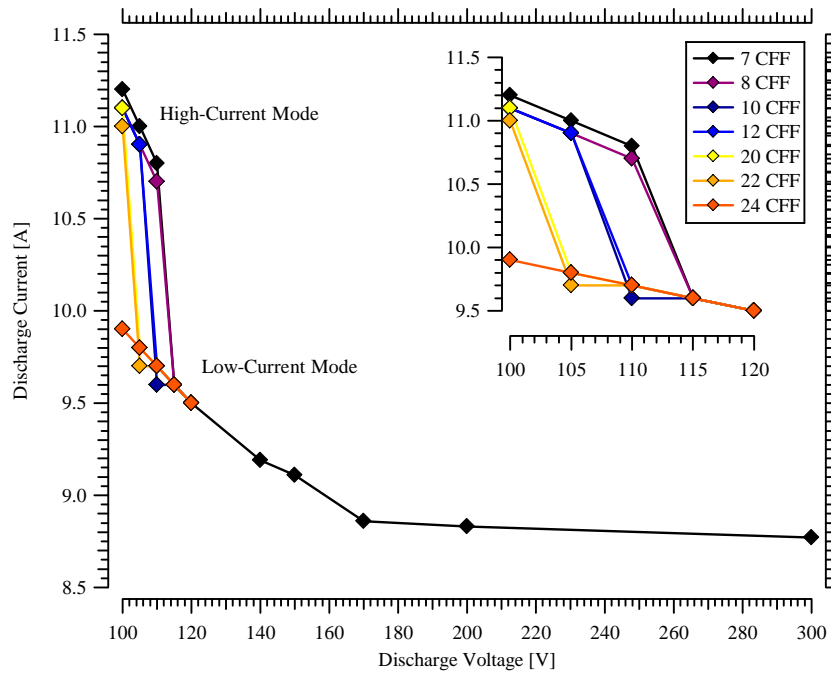


**Figure 9. Thruster I-V characteristics at 10-mg/s anode flow rate. Lines of constant cathode flow rate operation are shown as a function of discharge voltage from 100-V to 300-V. Low discharge voltage operation is magnified from 100-V to 120-V discharge.**

### B. Discharge Oscillations

In addition to a significant variation in the discharge current magnitude, the high-current mode may be identified by a significant increase in the amplitude of discharge oscillations. The substantial change in discharge current oscillation amplitude is shown in Figure 10 for 105-V, 20-mg/s, 16-CFF and 120-V, 10-mg/s, 7-CFF operation. The 105-V, high flow rate condition was chosen because it exhibited a large change in thruster performance between the high-current and low-current modes. The 120-V, 10-mg/s, 7-CFF case was chosen because it is opposite the 105-V case in terms of higher voltage, lower anode flow, and lower cathode flow fraction. For equivalent comparison of high-current and low-current operation, the hysteresis effect enabled identical magnetic field settings between operating regimes.

The power spectra of discharge current and cathode-to-ground potential oscillations are shown in Figure 11 for the 105-V case shown in Figure 10. Although the oscillation amplitude increased from low-current to high-current mode, the dominant frequency was constant. In addition, peak frequency of the discharge current oscillations match the cathode-to-ground potential

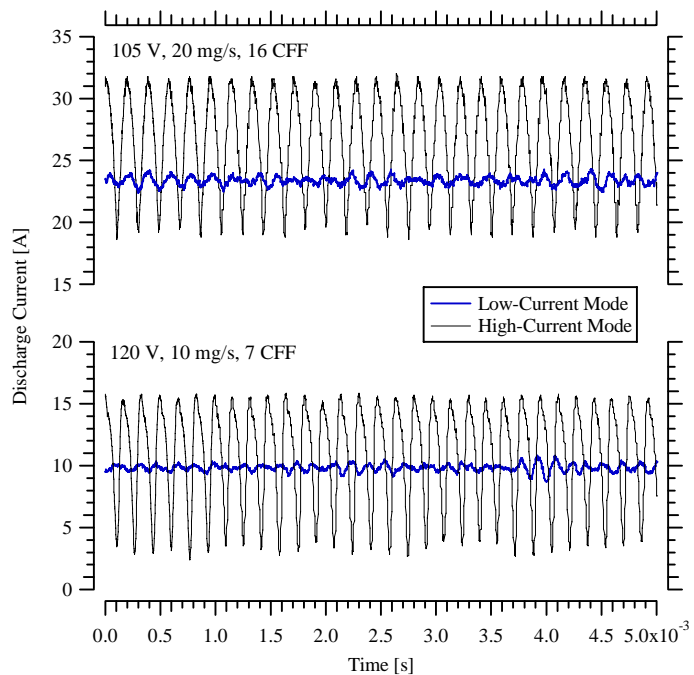


**Figure 10. Comparison of discharge current oscillations in the low-current and high-current modes for 105-V, 20-mg/s, 16-CFF operation during a 5-ms time period.**

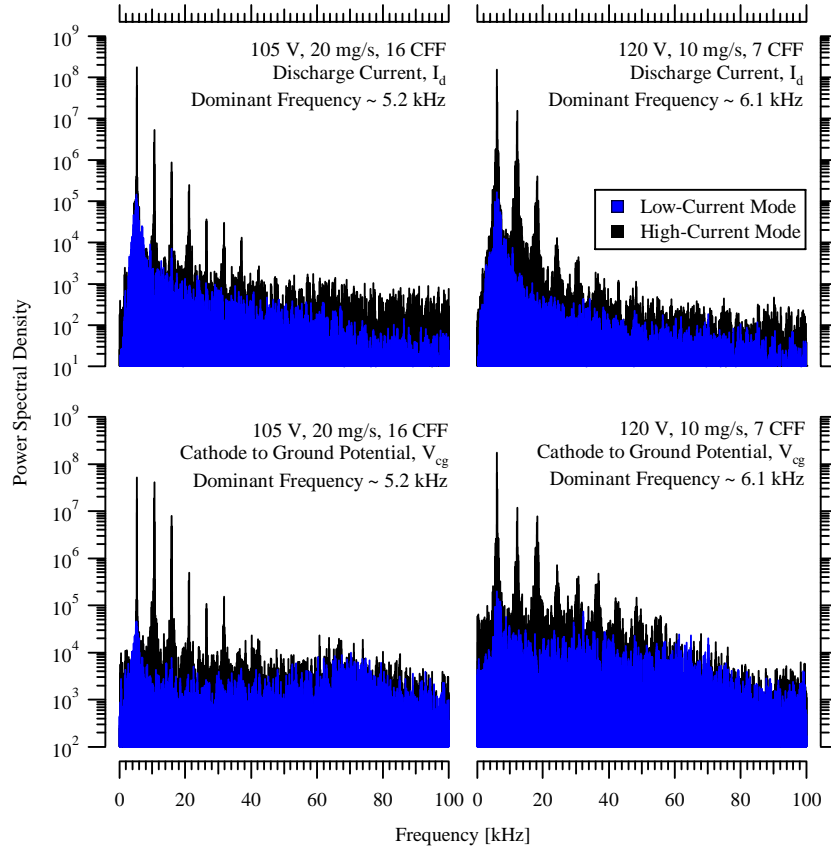


**Figure 11. Comparison of discharge current oscillation spectra (top) and cathode to ground potential oscillation spectra (bottom) in the low-current and high-current modes for 105-V, 20-mg/s, 16-CFF operation (left) and 120-V, 10-mg/s, 7-CFF operation (right) from 0 to 100-kHz.**

oscillations. Subsequent peaks are harmonics of the dominant frequency. These trends demonstrate there is significant cathode coupling during high-current operation. These trends are consistent with all oscillation measurements of the high-current and low-current regimes.

The stimulus of these oscillations is unknown. Possibilities include the Hall thruster breathing mode, the rotating “spoke” instability associated with low discharge voltage operation, oscillations manifested from cathode operation, or power supply induced discharge oscillations. The three former possibilities are associated with ionization instabilities. The constant frequency of oscillations between high-current and low-current modes indicates one of the instabilities is amplified. All four possibilities will be discussed in Section VI.

One key is that increased cathode flow eliminates the high-current operation, and may be due to increased neutral density near the thruster or cathode exit. In this case, increased facility background pressure should have a similar effect on the high-current operating regime. This is studied in Figure 12 for the 105-V, 20-mg/s, 16-CFF case and 120-V, 10-mg/s, 7-CFF case.

In the 105-V case, increased facility background pressure ranging from  $2.2 \times 10^{-5}$  to  $3.5 \times 10^{-5}$  torr did not affect the discharge oscillations. However, the 120-V case exhibited a 1-kHz increase in the dominant frequency and a reduction in magnitude of spectra harmonics. Further increasing the background pressure up to  $\sim 4.0 \times 10^{-5}$  torr caused the thruster to transition to the low-current operating regime, and is further evidence that increased neutral density near the exit minimizes the discharge oscillations.

Since the high-current operating regime of the 120-V, 10-mg/s, 7-CFF case appeared to be more sensitive to increased neutral density near the exit in Figure 12, this operating condition is studied in further detail for variations in CFF in Figure 13. The dominant frequency of the high-current mode increased from 5.8 kHz up to 6.3 kHz when cathode flow was increased from 5-CFF to 12-CFF. The low-current mode exhibited negligible variation in the dominant frequency as cathode flow fraction was increased.

The trends in performance and discharge oscillations indicate high-current operation is associated with amplification of ionization instabilities, and these instabilities may be minimized with additional neutral flow near the thruster exit. As demonstrated in Section IV.A, the primary effect on thruster performance was a decrease in the discharge current. Far-field plume properties will be studied in Section V to further examine the low discharge voltage Hall thruster operating regimes.

## V. Far-Field Plume Measurements

Examination of the far-field plume properties was conducted with a nude Faraday probe, RPA, Langmuir probe, and ExB probe. The 105-V, 20-mg/s, 16-CFF case will be used as a benchmark for the high-current and low-current modes due to the stable thruster operation in each regime over a wide range of background pressures. Variations in anode flow rate, cathode flow rate, and discharge voltage will be studied relative to this operating condition.

### A. Ion Beam Current and Plume Divergence

The angular distributions of ion current density at vacuum conditions for the low-current mode and high-current mode are shown in Figure 14. The benchmark 105-V, 20-mg/s, 16-CFF condition in each regime is evaluated with operation at 10-mg/s anode flow, with operation at 10-CFF, and with operation at 120-V discharge. The minimal cathode flow required for low-current mode is 10-CFF. Plume properties are listed in Table 2 to more clearly discern differences in the current density profiles.

The high-current mode was associated with a decrease in current utilization ( $I_{\text{Beam}}/I_d$ ), and therefore an increase in electron current to the anode in all cases. The increase in anode electron current suggests Joule heating losses and/or electron leakage to the anode are increased in the high-current mode.

The global result of the high-current mode appears to be increased beam divergence, increased anode electron current, and increased ion beam current. While these effects vary slightly depending on the thruster operation, it is consistent with an escalation of Joule heating losses in addition to ionization and/or an acceleration profile further downstream in the discharge channel.

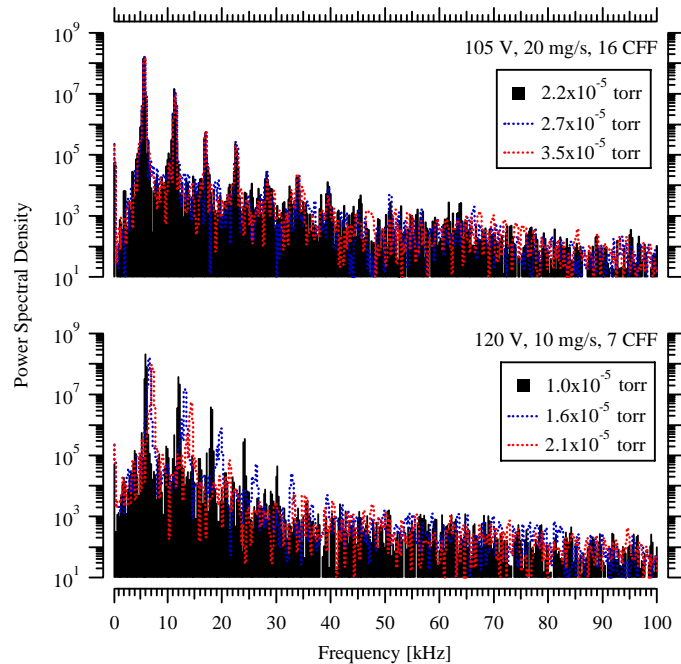


**Figure 12.** Comparison of discharge current oscillation spectra in the high-current mode for 105-V, 20-mg/s, 16-CFF operation (top) and 120-V, 10-mg/s, 7-CFF operation (bottom) with variation in facility background pressure.

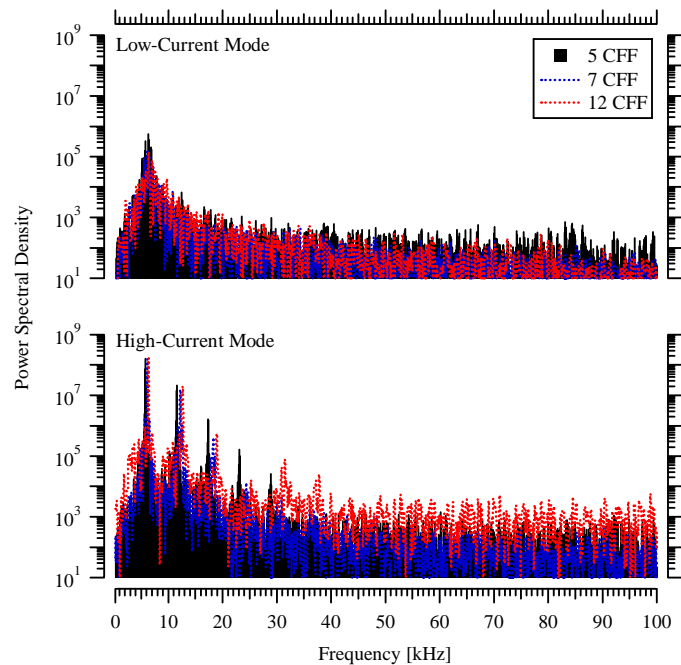


**Figure 13.** Comparison of discharge current oscillation spectra in the low-current mode (top) and high-current mode (bottom) for 120-V, 10-mg/s operation at 5, 7, and 12-CFF.

**Table 2. Comparison of the ion and electron currents in the discharge of the 6-kW Hall thruster during low-current and high-current operation.**

Operating Conditions	Operating Regime	Current [A]		Current Utilization, $I_{Beam}/I_d$	Divergence Half-Angle, $\lambda$ [degrees]
		$I_d$	$I_{Beam}$		
105-V, 20-mg/s, 16-CFF	Low-current	22.9	16.2	0.71	31°
105-V, 20-mg/s, 16-CFF	High-current	27.1	18.0	0.66	36°
105-V, 10-mg/s, 16-CFF	Low-current	10.0	6.8	0.68	34°
105-V, 10-mg/s, 16-CFF	High-current	12.0	7.7	0.64	33°
105-V, 20-mg/s, 10-CFF	Low-current	22.1	15.8	0.72	31°
105-V, 20-mg/s, 10-CFF	High-current	26.8	16.9	0.63	33°
120-V, 20-mg/s, 16-CFF	Low-current	22.6	16.6	0.74	28°
120-V, 20-mg/s, 16-CFF	High-current	25.9	16.6	0.64	33°

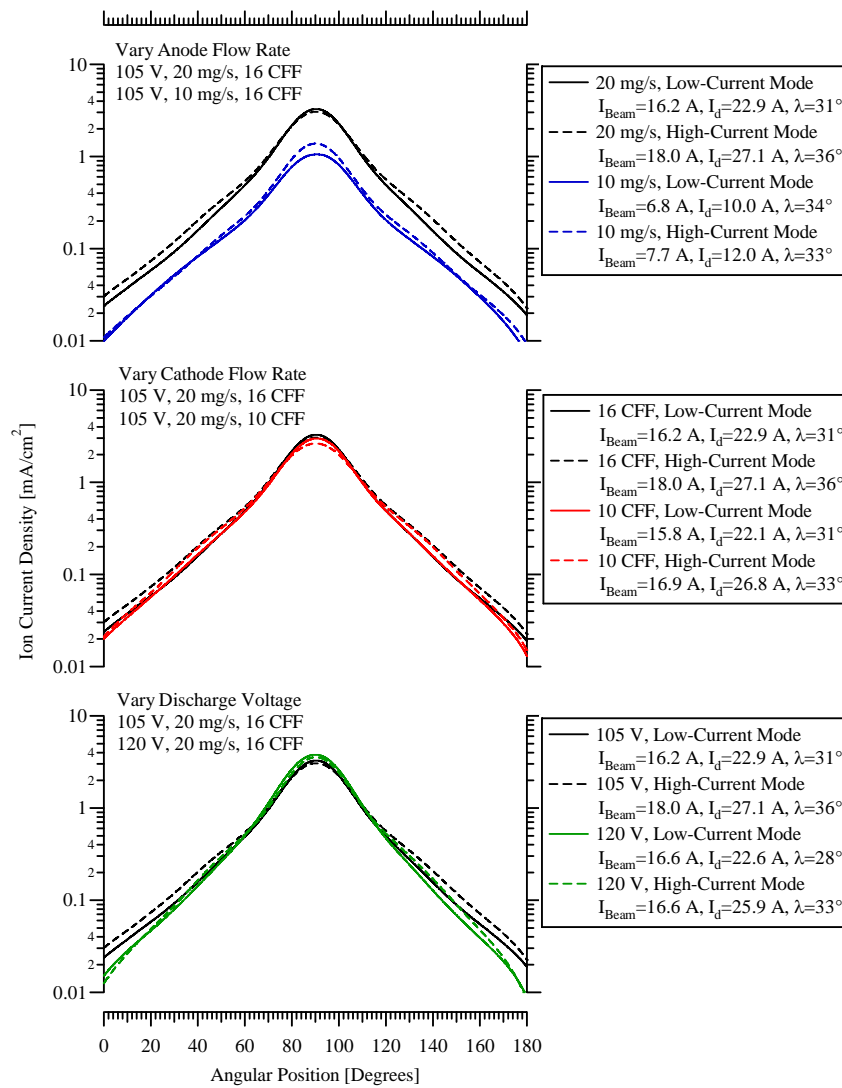


**Figure 14. Comparison of ion current density extrapolated to vacuum for high-current and low-current regimes. The current density at 105-V, 20-mg/s, 16-CFF is compared to the case of decreased anode flow at 10-mg/s (top), decreased cathode flow rate at 10-CFF (middle), and increased anode potential at 120-V (bottom).**

## B. Plasma Potential and Electron Temperature

Far-field Langmuir probe measurements on channel centerline are shown in Figure 15 for 105-V, 20-mg/s operation from 8-CFF to 16-CFF in the high-current and low-current modes. The trends in these profiles are representative of the other low-voltage operating conditions.

As cathode flow fraction was increased from 8-CFF to 10-CFF in the high-current mode, the location of peak  $dI/dV$  shifted left, indicating the far-field plasma potential decreased. At 10-CFF, the transition to low-current mode corresponded to a  $\sim 0.5$  V increase in plasma potential. Although the variations in plasma potential were within the measurement uncertainty, this trend was consistent for all operating conditions between the low-current and high-current regimes.

Electron temperature followed a similar trend with cathode flow fraction, as evidenced by the slope of the natural logarithm profile from approximately 2-V to 5-V bias potential in Figure 15. The increase in plasma potential during the transition to low-current mode was accompanied by an increase in the far-field electron temperature. The electron temperature varied by less than 1 eV during the transition, which was within the estimated measurement uncertainty.

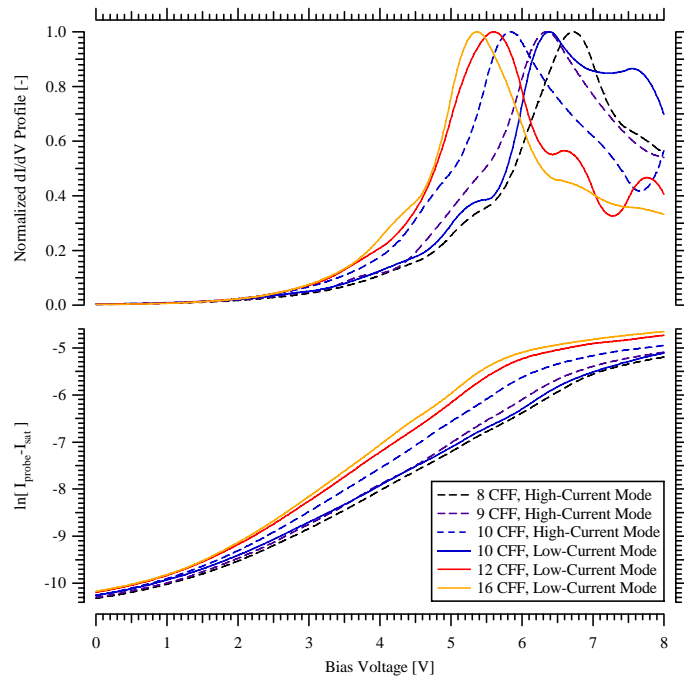


**Figure 15.** Langmuir probe traces of normalized  $dI/dV$  (top) and the natural logarithm (bottom) located 1-m downstream on thruster centerline for 105-V, 20-mg/s operation with cathode flow fraction ranging from 8-CFF to 16-CFF.

## C. Ion Energy per Charge Distributions

Thus far, the transition from the high-current to low-current regime has been associated with decreased electron current to the anode, with increased electron temperature, and increased plasma potential in the far-field plume. The operating modes will be further studied using RPA distributions of ion energy per charge on thruster centerline, corrected using the local plasma potential from Langmuir probe measurements.

In Figure 16, the RPA profile of ion energy per charge displays the most probable ion acceleration potential for 105-V, 20-mg/s operation from 8-CFF to 16-CFF. Variation in cathode flow had a negligible effect on the most probable ion acceleration potential, and appeared to have a minimal effect on the beam ion acceleration. The most significant variations occur on the high energy side of the ion energy per charge profile between 90-V and 140-V. Ions with energy per charge ratio greater than the most probable ion acceleration potential are typically attributed to propellant ionized near the anode face or to multiply-charged ions that experienced a charge-reducing CEX collision downstream of the acceleration zone, thereby generating a high

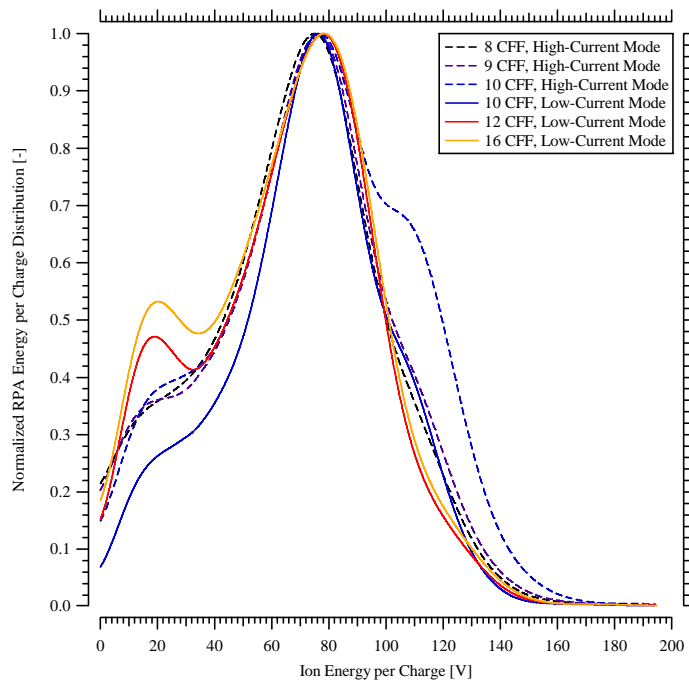


**Figure 16.** Normalized RPA ion energy per charge distributions located 1-m downstream on thruster centerline for 105-V, 20-mg/s operation with cathode flow ranging from 8-CFF to 16-CFF. The distribution has been corrected for local plasma potential.

energy  $Xe^+$ . Thruster operation from 8-CFF to 10-CFF exhibited a substantial fraction of the energy per charge distribution greater than the discharge voltage, which would imply the high energy ions were at one time multiply-charged. The effect is exacerbated at 10-CFF in the high-current mode, at the transition to the low-current operating regime. Secondary peaks in the ion energy per charge distribution located at  $\sim 20$  V are most likely due to space-charge limitations between the RPA grids. Insensitivity of the most probable ion acceleration potential with cathode flow fraction displayed in Figure 16 was representative of the other low-voltage operating conditions. Voltage utilization varied by less than 2% with variations in cathode flow fraction.

#### D. Ion Energy Distributions

In Figure 17, ion energy distributions of the benchmark 105-V, 20-mg/s, 16-CFF operation in the high-current and low-current regimes is evaluated with operation at 10-mg/s anode flow, with operation at 10-CFF, and with operation at 120-V discharge. In the high-current operating regime, the ion energy distributions show significant deviations from the distribution of the nominal low-current mode. These variations were extremely repeatable and exhibited minimal variation with downstream distance from 1.0 to 1.3-meters. The uncertainty of ion energy distributions in the high-current mode are estimated as equal to the low-current mode.

Examination of the benchmark 105-V, 20-mg/s, 16-CFF operation shows that the primary  $Xe^+$  peak is drastically reduced in magnitude during high-current operation. The peak of the high-current regime profile occurs between the  $Xe^+$  peak and the  $Xe^{+2}$  peak of the low-current regime. The radical transformation of the ion energy distribution indicates a significant number of ionization processes are occurring in the discharge. Extracting quantitative information about the ion species composition from these distributions is not possible. Instead, the ion energy distributions will be used for a qualitative comparison between operating regimes and between thruster operating parameters.

The ion species current fractions were 0.92  $Xe^+$  ions and 0.08  $Xe^{+2}$  ions for the 20 mg/s anode flow conditions during low-current mode operation. During the 105-V, 10 mg/s case the ion species current fractions were 0.96  $Xe^+$  ions and 0.08  $Xe^{+2}$  ions. While no  $Xe^{+3}$  ion peaks were detected in the low-current mode, a significant fraction of high energy ions greater than  $Xe^{+2}$  ions were seen in the high-current mode ion energy distributions. Although the primary peak is likely a combination of high energy  $Xe^+$  ions and low energy  $Xe^{+2}$  ions, the ion energy distributions are difficult to compare when the ion species velocities overlap and the relative magnitude varies depending on the charge state. Comparison of these profiles is limited without estimating the contribution of each species to the overall distribution.

#### E. Comparison of Ion Energy per Charge Distributions

To more accurately assess the fraction of multiply-charged ions compared to high energy  $Xe^+$  ions, the ion energy distribution of the 105-V, 20-mg/s, 10-CFF case for high-current and low-current mode will be decomposed into energy distributions of the individual ion species. In Figure 18, the ExB probe ion energy distributions are

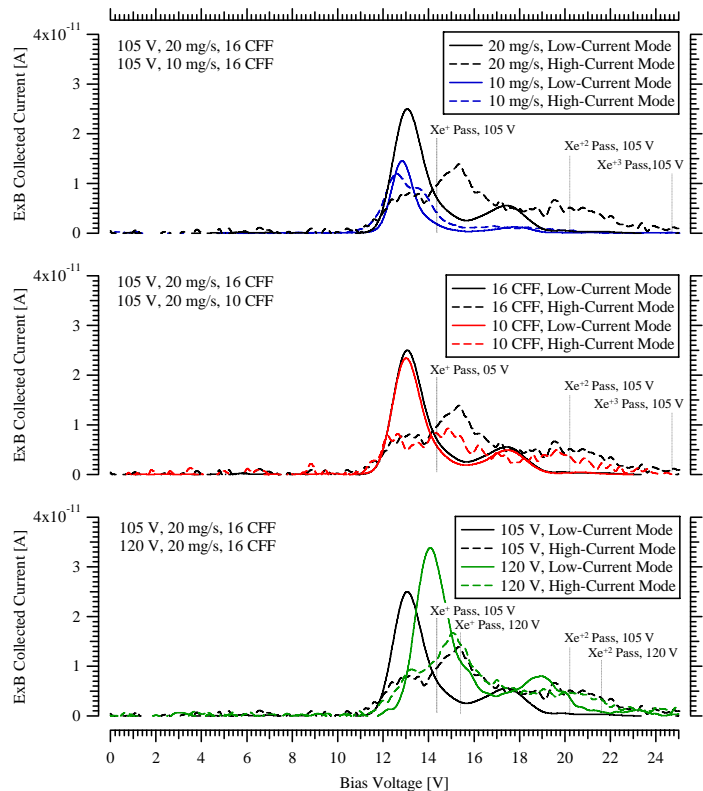


**Figure 17. Comparison of ExB probe ion energy distributions on channel centerline located 1-meter downstream of the exit plane for high-current and low-current regimes. The ion energy distribution at 105-V, 20-mg/s, 16-CFF is compared to the case of decreased anode flow at 10-mg/s (top), decreased cathode flow rate at 10-CFF (middle), and increased anode potential at 120-V (bottom). The ion species pass velocity for maximum acceleration over the anode discharge voltage is shown for comparison, and does not account for additional ion acceleration from plasma potential to the ground reference at the probe entrance.**

normalized according to the peak of the low-current operating mode, and partitioned into ion species distributions of  $Xe^+$  ions and  $Xe^{+2}$  ions. To match the scaling of multiply charged ions in RPA ion voltage distributions and ExB ion energy distributions, the magnitude of the ExB  $Xe^{+2}$  ion distribution is approximately proportional to  $Z_j^{1/2} V_d$  according to Eq. (4) and Eq. (6). In addition, the ExB pass voltage of  $Xe^{+2}$  ions has been corrected for the increased velocity due to higher charge state.

The location where the ion energy distribution was divided is somewhat arbitrary, but was chosen based on an iterative approach to match the low energy side of the combined ion energy per charge distribution of the high-current and low-current regimes. The separation point is labeled on the figure for each operating regime. This matching of low energy distributions is comparable to the RPA ion energy per charge measurements. The ion pass voltage of the RPA and ExB distributions have been corrected for local plasma potential near the RPA, and differences in the plasma properties surrounding the ExB probe are considered minor compared to the large uncertainty associated with this qualitative examination. Superposition of  $Xe^+$  and  $Xe^{+2}$  ion energy per charge distributions from ExB measurements produced reasonable agreement with RPA measurements of energy per charge in Figure 18.

The distributions of ion energy and ion energy per charge will aid in the assessment of low discharge voltage operating regimes, and enable a more comprehensive evaluation of the beam composition. Two mechanisms may contribute to the observed transformation of ion energy and ion energy per charge distributions during operation in the high-current regime. The first mechanism involves two distinct primary beam ion populations fluctuating in time with the discharge oscillations. The  $Xe^+$  ion species energy per charge distribution indicates there may be two distinct peaks in this population. One population is associated with ionization at approximately the same point in the potential field as the nominal low-current regime. The second population would correspond to ionization closer to the anode face and further upstream of the applied potential profile. Although not as distinct, the  $Xe^{+2}$  ion species energy per charge distribution also exhibits the possibility of two populations. Although the ions may be accelerated over a larger potential field, these populations would not be expected to produce ions with energy per charge greater than the discharge voltage.

The second source for generation of high energy ions is due to charge-reducing CEX collisions of multiply-charged ions downstream of the primary acceleration region. This would create two distinct populations in space, but would necessitate a large fraction of  $Xe^{+3}$  ions in the discharge channel and subsequent CEX collisions to create a population of high energy  $Xe^{+2}$  ions. This mechanism for production of high energy  $Xe^{+2}$  ions is expected to have an extremely low probability, and therefore would indicate the first mechanism is more likely.

For this operating condition, it is believed that the large dispersion in ion species energy per charge distributions during high-current operation is caused by variations in the ionization zone relative to the acceleration profile. The large ionization instabilities and current oscillations

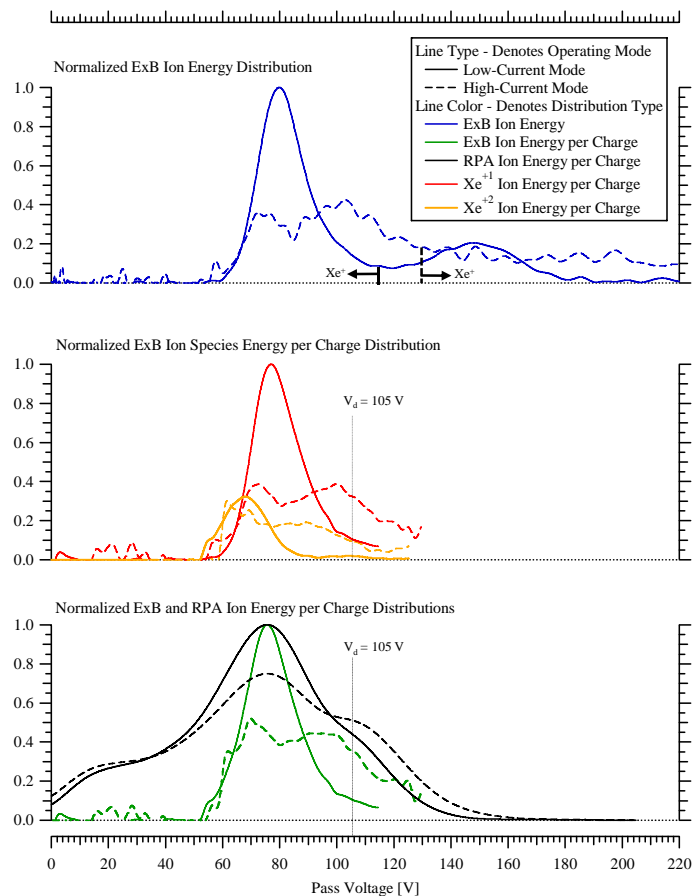


**Figure 18.** Comparison of ExB probe and RPA measurements on channel centerline located 1-meter downstream of the exit plane for 105-V, 20-mg/s, 10-CFF operation in the high-current and low-current regimes. The ExB probe ion energy distributions (top), ExB probe ion species energy per charge distributions (middle), and the comparison of RPA and ExB probe ion energy per charge distributions (bottom) are normalized to the peak of the low-current profile for each diagnostic.

lead to the cyclic exhaust and resupply of neutral propellant in the discharge. Electron current to the anode increased during the high-current mode, and may be due to electron leakage to the anode or to sustain ionization processes. Thrust may be approximately constant if a comparable fraction of propellant is accelerated over the most probable potential profile during one discharge oscillation.

Based on the hypothesis that the ion energy distribution is created by the discharge oscillations and an increase in fraction of multiply-charged ions, the effect of increased neutral density near the thruster exit will be evaluated in Section V.F.

### F. Variation in Near-field Neutral Density

In Section IV.A, the low discharge voltage operating regimes were studied with variations in the cathode flow fraction. Due to the sensitivity to the near-field neutral density, a second method of evaluating increased neutral density near the thruster exit is by injecting a fraction of the cathode flow through an auxiliary port, as illustrated in Figure 19. Auxiliary flow was injected around the keeper to study whether the low-voltage discharge behavior was due to processes internal to the cathode or external to the cathode exit. The auxiliary flow serves to increase the flow surrounding the cathode keeper and is expected to create a more diffuse cloud of neutral propellant. This thruster operation was studied in detail using the far-field diagnostics and characterized with variations in facility background pressure to determine the performance in vacuum. The 105-V, 20-mg/s, 10-CFF operating condition was studied for the case of 5-CFF and 2-CFF, where the remaining flow fraction was injected through the auxiliary port such that the total mass flow rate was equivalent to 10-CFF. The 10-CFF case was chosen since it is the minimum cathode flow rate required for operation in the low-current regime at 105-V, 20-mg/s.

Variations in thruster performance with auxiliary flow injection are characterized with background pressure and displayed in Figure 20. At vacuum conditions, the total efficiency is reduced by approximately 1% for operation at 2-CFF. However, operation in the low-current regime would not be possible for this low cathode flow fraction without the auxiliary flow rate of 8-CFF surrounding the keeper. Based on plume diagnostics, the decreased performance with auxiliary flow and reduced cathode flow fraction is associated with a minimal increase in current utilization and a decrease in beam divergence.

In the low-current regime, operation at each auxiliary flow condition demonstrated relatively constant T/P with decreasing background pressure, and is likely due to a constant neutral entrainment area. Conversely, the high-current regime shows significant reductions in performance at vacuum. This is attributed to the

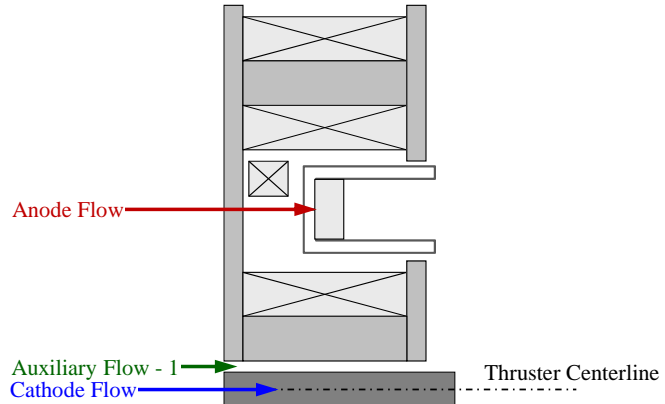


**Figure 19. Schematic of the 6-kW laboratory model Hall thruster illustrating locations of propellant injection at the anode, cathode, and auxiliary port.**

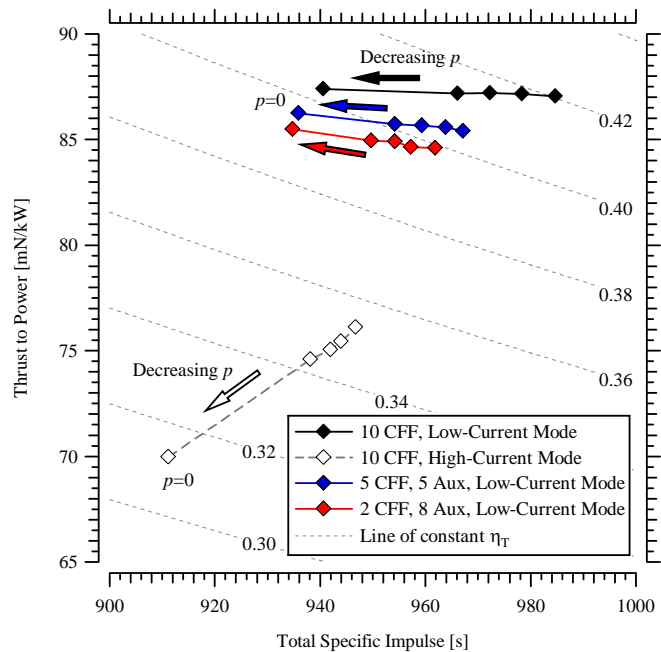


**Figure 20. Ratio of thrust T/P and total Isp with variation in cathode flow and auxiliary propellant for 105-V, 20-mg/s operation in the high-current and low-current regimes. The total combined flow to the cathode and auxiliary port is fixed and equivalent to 10-CFF, such that the total mass flow to the thruster is constant. Performance parameters are extrapolated to vacuum conditions.**

reduction in neutral propellant available to minimize the discharge oscillations, and is likely caused by a greater fraction of electron current to the anode.

The primary advantage of the auxiliary flow injection was to enable a wider operational envelope where the thruster could operate in the low-current regime. This included both magnetic field topography and cathode flow rate. In this study, the magnetic field was held constant. However, performance and beam divergence may improve with optimized magnet settings. For this operating condition, the auxiliary flow could be reduced to 7-CFF when 2-CFF was supplied to the cathode. Although this did not improve performance, the addition of auxiliary flow may be considered a safeguard to maintain low discharge voltage operation in the low-current regime. Just as the high-current mode may be mitigated at increased background pressures, it may arise on-orbit in the vacuum of space for operating conditions that did not cause the high-current mode in ground-based experiments with a finite facility background pressure. Further study is required to more accurately characterize the thruster operation and discharge properties with auxiliary flow. An accurate study of facility background pressure effects would be critical for this examination.

## VI. Discussion

The presence of two discharge current regimes was demonstrated to be a low-voltage phenomenon. As previously stated, discharge oscillations in the high-current mode may be caused by (1) breathing mode oscillations, (2) the azimuthal rotating “spoke” instability, (3) cathode induced instabilities, or (4) discharge power supply instabilities. Each scenario will be evaluated and discussed in the following sections.

### A. Thruster Ionization Instabilities

A constant discharge frequency between the low-current and high-current operating regimes indicates that the oscillations are a natural phenomena of the discharge that is driven unstable by a local depletion of neutral density near the exit. The dominant frequency of  $\sim 5$  kHz is within the frequency range of the breathing mode oscillations and the azimuthal “rotating spoke” instability described by Choueiri.<sup>3</sup>

The rotating spoke oscillations arise during low discharge voltage operation, and are generated by coupling between ionization processes and density non-uniformities in the channel. These instabilities were observed during the early years of Hall thruster research, and were believed to correspond to an azimuthal disturbance on the order of the critical ionization velocity (4.2-km/s for xenon).<sup>17</sup> For the 6-kW thruster in this investigation, the critical ionization velocity of xenon would correspond to an azimuthal cycle around the annulus on the order of  $\sim 8$  kHz.

The dominant breathing mode frequency during nominal Hall thruster operation is the breathing-mode frequency, and is due to the cyclic exhaust and resupply of neutral propellant near the exit. These oscillations are known to result in severe discharge fluctuations and show a dependence on the magnetic field. Based on the “predator-prey” model, the breathing mode frequency is estimated at  $\sim 7$  kHz for the 6-kW thruster in this investigation during low discharge voltage operation ( $<120$ -V).

Recent time-resolved studies of the BHT-600 Hall thruster discharge showed discrete toroidal plasma emissions corresponding to the breathing mode frequency.<sup>18</sup> Regions between the dense plasma structures contained approximately 75% lower plasma density during nominal 200-V discharge operation. The electron temperature and plasma potential varied with the breathing mode oscillations, and appeared to be driven by electron dynamics and the electromagnetic field. The resulting fluctuations and gradients in plasma potential associated with the propagating toroidal plasma may be a significant fraction of the anode potential during low-voltage operation.

Both the breathing mode oscillations and the spoke instabilities are related to ionization processes near the thruster exit, and the coupling between these oscillations is unknown. The mechanism for electron current to the anode and the nature of cross-field electron transport is beyond the scope of this investigation. The concept of discrete toroidal plasma emissions and the interactions of intense ionization instabilities external to the discharge channel necessitate simulation of the electron dynamics and a more sophisticated interrogation of the near-field region.

### B. Cathode Induced Discharge Oscillations

Low-voltage Hall thruster operation may be more susceptible to cathode coupling effects due to the increased fraction of propellant ionization cost and cathode-to-ground potential with respect to the applied anode potential. Furthermore, the results of this study indicate the thruster may be more sensitive to ionization instabilities and plasma potential fluctuations near the thruster exit during low-voltage operation.

The thruster sensitivity to cathode flow indicates the transition between high-current and low-current regimes may be triggered by cathode coupling or a cathode operating effect. One possibility is the gradual transition from

cathode spot-mode to plume-mode, which is a function of cathode flow rate, the local magnetic field, and plasma properties near the exit orifice. Cathode plume-mode operation is associated with an increase in electron temperature, cathode coupling voltage, and plasma potential oscillations near the cathode exit.<sup>19,20,21</sup> Plasma potential oscillations and energetic ion production during cathode plume-mode are the result of ionization instabilities near the cathode exit plane.<sup>22</sup> These instabilities typically increase with decreasing cathode flow and off-nominal magnetic field.

A recent investigation by Goebel, *et al.*<sup>22</sup> reported that large plasma potential oscillations and energetic ion production in the near-cathode region may be reduced by increased cathode flow or injection of neutral gas downstream of the cathode exit plane. It was surmised that cold neutral flow either damped the large potential oscillations and/or produced additional ionization to reduce the instabilities. In the low discharge voltage investigation in this dissertation, increased neutral density near the cathode exit may have mitigated the cathode induced plasma potential oscillations and stabilized the ionization instabilities. This moderation resulted in low-current thruster operation. Similar to the study by Goebel, auxiliary neutral flow injection near the cathode exit plane enabled a lower cathode flow rate required to maintain low-current thruster operation. This supports the concept of cold, dense neutral flow in the near-cathode region stabilizing plasma oscillations and instabilities, and increasing the thruster and cathode operational envelope.

It is uncertain whether the thruster operation coincides with the cathode transition from spot-mode to plume-mode. The high-current mode in Figure 1 exhibited an intense, collimated plume extending into the cathode, which is characteristic of the plume-mode operation. In comparison, the low-current mode in Figure 1 showed a luminous spot of intense ionization near the cathode orifice, indicative of the spot-mode operation. Although the cathode potential and discharge current oscillations were fluctuating at the same frequency in high-current regime, it remains unclear if this is a cause or consequence of the plasma discharge oscillations. Further cathode characterization and examination of the near-cathode electron temperature and plasma potential is necessary to determine the cathode operating envelope during Hall thruster operation. Regardless of the specific cathode operating mode, plasma potential oscillations and energetic ion production have been shown to increase as cathode flow is reduced. Therefore, a critical magnitude of plasma perturbations near the cathode exit may affect thruster performance prior to the onset of plume-mode operation.

Several issues develop if the cathode operation is responsible for transition between the low discharge voltage operating regimes. The centrally-mounted cathode is surrounded by the iron magnetic circuit and is located in a region with minimal axial magnetic field. Although cathode operation has shown sensitivity to the axial magnetic field in past studies, it seems unlikely that the minimal variation in magnetic field topography would have a strong influence on the magnetic field in this region. Past cathode coupling studies performed on the BPT-4000<sup>23</sup> and also with this thruster model<sup>10</sup> at discharge voltage >300-V concluded cathode flow rate had a negligible effect on performance. A more systematic study is required to determine if the cathode operating condition is affecting low discharge voltage performance and initiating severe discharge oscillations in the high-current regime.

### **C. Discharge Power Supply Oscillations**

Extensive investigations in the former Soviet Union established that the Hall thruster discharge oscillations may be affected by the external supply and electrical circuit.<sup>1,2</sup> In this investigation, a ~500 Hz RLC filter was removed from the circuit with negligible change in the low-voltage thruster operation or discharge characteristics. While it does not rule out oscillations induced by the discharge power supply, it suggests that the operating regimes are a low discharge voltage plasmadynamic phenomenon associated with the thruster or cathode. In addition, a qualitative assessment of the low-voltage characteristics of this thruster model at PEPL demonstrated features in discharge current magnitude and oscillations that were consistent with the low-current and high-current operating regimes. Differences between facilities may be attributed to a different thruster model, discharge power supply circuitry, or variation in the centrally mounted cathode.

## **VII. Summary**

A systematic mapping of low discharge voltage Hall thruster performance revealed the existence of two jet-mode operating regimes. The regimes were classified as high-current mode and low-current mode, and corresponded to a visible transformation of the jet-mode plume structure. The low-current mode corresponded to the I-V characteristic of nominal discharge voltage operation, whereas operation in the high-current mode produced significant increases in the discharge current magnitude and oscillation amplitude. A large increase in the amplitude of discharge current oscillations manifested as a ~10% increase in the discharge current magnitude. The regimes were characterized through a systematic mapping of low discharge voltage Hall thruster performance with variations in the applied

anode-to-cathode potential, anode mass flow rate, and cathode mass flow rate. The discharge regimes were highly dependent on cathode coupling and magnetic field topography.

Evaluation of the thruster performance and far-field plume demonstrated that electron current to the anode was the primary source of increased discharge current in the high-current regime. Analysis of the ion energy distributions and ion energy per charge distributions revealed that the high-current regime corresponded to increased multiply-charged ions and wide dispersion in the ion species energy distributions. This phenomenon may be caused by the cyclic exhaust and resupply of neutral propellant in the discharge. Increased neutral flow to the near-cathode region by additional cathode flow injection, through an auxiliary port, or by increased facility background pressure was shown to enable thruster operation in the more efficient low-current mode. A qualitative assessment of potential causes led to the hypothesis that the high-current operating mode is a result of (1) instability associated with the breathing mode and/or the rotating spoke instability, or (2) instability initiated by large radial plasma potential fluctuations and ionization instabilities near the cathode exit due to operation in the cathode plume-mode. The high-current mode discharge oscillations declined with increased neutral flow near the thruster exit, and eventually enabled operation in the low-current regime. Conversely, oscillations in the high-current regime were amplified as neutral density in the near-field was decreased with facility background pressure. Injection of additional auxiliary flow in the thruster near-field is recommended as a safeguard to maintain low discharge voltage operation in the low-current regime, and reduce the possibility of operation in the high-current regime on-orbit. Although the exact nature of the low-voltage operating regimes remains uncertain, the discharge characteristics are systematically evaluated and mitigation strategies are demonstrated.

## References

- <sup>1</sup> Tilinin, G., *Sov. Phys. Tech. Phys.*, 22, 974, 1977.
- <sup>2</sup> Esipchuck, Y., Morozov, A., Tilinin, G., Trofimov, A., *Sov. Phys. Tech. Phys.*, Vol. 18, pp. 928, 1974.
- <sup>3</sup> Choueiri, E. Y., "Plasma Oscillations in Hall Thrusters," *Physics of Plasmas*, Vol. 8, No. 4, April 2001.
- <sup>4</sup> Chesta, E., Lam, C. M., Meezan, N. B., Schmidt, D. P., Cappelli, M. A., "A Characterization of Plasma Fluctuations within a Hall Discharge," *IEEE Transactions on Plasma Science*, Vol. 29, No. 4, August 2001.
- <sup>5</sup> Azziz, Y., "Experimental and Theoretical Characterization of a Hall Thruster Plume," Doctoral Dissertation, Department of Aeronautics and Astronautics, Massachusetts Institute of Technology, Cambridge, MA, 2007.
- <sup>6</sup> Meezan, N. B., Hargus Jr., W. A., Cappelli, M. A., "Optical and Electrostatic Characterization of Oscillatory Hall Discharge Behavior," AIAA Paper 98-3502, 1998.
- <sup>7</sup> Gascon, N., Perot, C., Bonhomme, G., Caron, X., Bechu, S., Lasgorceix, P., Izrar, B., Dudeck, M., "Signal Processing and Non-Linear Behavior of a Stationary Plasma Thruster: First Results," AIAA Paper 99-2427, 1999.
- <sup>8</sup> Brown, D. L., "Investigation of Low Discharge Voltage Hall Thruster Characteristics and Evaluation of Loss Mechanisms," Doctoral Dissertation, Department of Aerospace Engineering, University of Michigan, Ann Arbor, MI, 2009.
- <sup>9</sup> Reid, B. M., "The Influence of Neutral Flow Rate in the Operation of Hall Thrusters," Doctoral Dissertation, Department of Aerospace Engineering, University of Michigan, Ann Arbor, MI, 2009.
- <sup>10</sup> Jameson, K. K., "Investigation of Hollow Cathode Effects on Total Thruster Efficiency in a 6-kW Hall Thruster," Doctoral Dissertation, Department of Aerospace Engineering, University of California, Los Angeles, CA, 2008.
- <sup>11</sup> Haag, T. W., "Thrust Stand for High-Power Electric Propulsion Devices," *Review of Scientific Instruments*, Vol. 62, No. 5, May 1991, pp. 1186-1191.
- <sup>12</sup> Brown, D. L., Gallimore, A. D., "Evaluation of Plume Divergence and Facility Effects on Far-Field Faraday Probe Current Density Profiles," IEPC-2009-074, 2009.
- <sup>13</sup> Gulszinski, F. S., "Examination of the Structure and Evolution of Ion Energy Properties of a 5 kW Class Laboratory Hall Effect Thruster at Various Operational Conditions," Doctoral Dissertation, Department of Aerospace Engineering, University of Michigan, Ann Arbor, MI, 1999.
- <sup>14</sup> Hutchinson, I. H., *Principles of Plasma Diagnostics*, 2<sup>nd</sup> Edition, Cambridge Univ. Press, New York, 1990.
- <sup>15</sup> Farnell, C. C., Brown, D. L., Willis, G., Branam, R., Williams, J. D., "Remote Diagnostic Measurements of Hall Thruster Plumes," IEPC-2009-031, 2009.
- <sup>16</sup> Shastry, R., Hofer, R. R., Reid, B. M., Gallimore, A. D., "Method for Analyzing ExB Probe Spectra from Hall Thruster Plumes," AIAA Paper 2008-4647, 2008.
- <sup>17</sup> Janes, G. S., Lowder, R. S., *Phys. of Fluids*, Vol. 9, pp. 1115, 1962.

- 
- <sup>18</sup> Lobbia, R. B., Gallimore, A. D., “A Method of Measuring Transient Plume Properties,” AIAA Paper 2008-4650, 2008.
- <sup>19</sup> Foster, J. E., Williams, G. J., Patterson, M. J., “Characterization of an Ion Thruster Neutralizer,” *Journal of Propulsion and Power*, Vol. 23, No. 4, July-August 2007.
- <sup>20</sup> Yu-Cai, F., Wilbur, P.J., “The Influence of Stray Magnetic Fields on Ion Beam Neutralization,” IEPC-82-1945, 1982.
- <sup>21</sup> Patterson, M.J., Mohajeri, K., “Neutralizer Optimization,” IEPC-91-151, 1991.
- <sup>22</sup> Goebel, D. M., Jameson, K. K., Katz, I., Mikellides, I. G., “Plasma Potential Behavior and Plume Mode Transitions in Hollow Cathode Discharges,” IEPC-2007-277, 2007.
- <sup>23</sup> Tilley, D. L., de Grys, K. H., Myers, R. M., “Hall Thruster – Cathode Coupling,” AIAA Paper 99-2865, 1999.